JAMES | Journal of Advances in Modeling Earth Systems

RESEARCH ARTICLE
10.1029/2019MS001853

On the Causal Relationship Between the Moist Diabatic Circulation and Cloud Rapid Adjustment to Increasing CO_2

T. Dinh[1] **and S. Fueglistaler**[2,3]

[1]Department of Physics, University of Auckland, Auckland, New Zealand, [2]Program in Atmospheric and Oceanic Sciences, Princeton University, Princeton, NJ, USA, [3]Department of Geosciences, Princeton University, Princeton, NJ, USA

Key Points:

- The hydrologic cycle weakens during rapid adjustment due to a reduction in tropospheric radiative cooling associated with CO_2 increase
- The mass of cloud condensates decreases during rapid adjustment as the production of condensates decreases in a weakened hydrologic cycle
- The decrease in cloud condensates is predicted from the decrease in the radiative subsidence mass flux of the moist diabatic circulation

Correspondence to:
T. Dinh,
t.dinh@auckland.ac.nz

Citation:
Dinh, T., & Fueglistaler, S. (2019). On the causal relationship between the moist diabatic circulation and cloud rapid adjustment to increasing CO_2. *Journal of Advances in Modeling Earth Systems*, *11*, 3836–3851. https://doi.org/10.1029/2019MS001853

Received 4 AUG 2019
Accepted 24 OCT 2019
Accepted article online 8 NOV 2019
Published online 26 NOV 2019

Abstract General circulation models predict that clouds in the atmosphere rapidly adjust to the radiative perturbation of an abrupt increase in atmospheric CO_2 concentration on a short time scale of about 10 days. This rapid adjustment consists of an increase of clouds in the boundary layer and a decrease of clouds in the free troposphere. Our focus is the mechanism for the decrease of clouds in the free troposphere, which is the dominating component of cloud rapid adjustment in most general circulation models. We propose that the decrease in clouds in the free troposphere arises from the causal relationship between the moist diabatic circulation and the production of condensates that forms clouds in moist processes. As CO_2 concentration increases, tropospheric radiative cooling is reduced, resulting in weakening of the moist diabatic circulation and a decrease in precipitation. As the hydrologic cycle weakens and the moist processes involving phase change of water vapor to form the condensates in the atmosphere lessen, the mass of cloud condensates decreases. This decrease in cloud condensates can be predicted from the decrease in the radiative subsidence mass flux, which is a metric for the strength of the moist diabatic circulation in the free troposphere.

Plain Language Summary Climate models predict that the global average precipitation and clouds decrease rapidly on a short time scale of about 10 days following an abrupt increase in atmospheric CO_2 concentration. We demonstrate that these rapid decreases in global precipitation and clouds are manifestations of the weakening of the hydrologic cycle, which is directly forced by the perturbation of the atmosphere's radiative energy budget due to CO_2 increase.

1. Introduction

Following an increase in CO_2 concentration, the perturbation in the atmosphere's radiative energy budget directly drives rapid adjustment processes (terminology following Gregory & Webb, 2008; Gregory et al., 2004) which re-establish energetic equilibrium for the atmosphere. Rapid adjustment takes place in the atmosphere on a very different time scale from the slow (decades to centuries) surface temperature changes because of the vast difference between the heat capacities of the atmosphere and the oceans. In the stratosphere, temperature adjustment restores pure radiative equilibrium on a time scale of about a month, which is set by the radiative heating rate perturbation and the heat capacity of the air. In the troposphere, energetic equilibrium is restored even more rapidly (within about 10 days, Dinh & Fueglistaler, 2017; Dong et al., 2009) predominantly through circulation change, with Newtonian radiative relaxation being significant only in the boundary layer (Dinh & Fueglistaler, 2017). The weakened circulation (Bony et al., 2013; Merlis, 2015) drives a hydrologic cycle with smaller latent and sensible heat fluxes (Andrews & Forster, 2010; Cao et al., 2012; Dinh & Fueglistaler, 2017; Dong et al., 2009). The decreases in latent and sensible heat fluxes at the surface are the pathway through which the perturbation in the radiative energy budget at the top of the atmosphere (TOA) is communicated to the surface (Dinh & Fueglistaler, 2017).

Additionally, rapid adjustment includes cloud changes. Cloud rapid adjustment, together with atmospheric temperature and water vapor adjustments, affects the net incoming radiative flux at the TOA, effectively modifying the forcing that drives surface warming. Accounting for rapid adjustment processes including clouds is necessary to ensure correct calculation of the effective forcing (terminology following Gregory et al.,

2004) and interpretation of transient and equilibrium climate sensitivity (e.g., Bala et al., 2009; Gregory & Webb, 2008; Gregory et al., 2004; Pincus et al., 2016). Across general circulation models (GCMs), the total cloud rapid adjustment is generally a decrease in cloud amount (Gregory & Webb, 2008; Kamae & Watanabe, 2012; Kamae et al., 2015; Webb et al., 2013; Zelinka et al., 2013), which decreases the reflected shortwave flux at the TOA and increases the outgoing longwave flux. In most GCMs the shortwave effect dominates such that cloud rapid adjustment contributes positively to the effective CO_2 forcing. The magnitude of this contribution is on the order of 1 W m^{-2} for a quadrupling of CO_2 concentration but with significant inter-model spread (Andrews & Forster, 2008; Kamae & Watanabe, 2012; Vial et al., 2013; Zelinka et al., 2013).

The amount and spatial structure of cloud rapid adjustment differ among GCMs (Gregory & Webb, 2008; Kamae & Watanabe, 2012; Webb et al., 2013; Zelinka et al., 2013). However, as emphasized by Kamae et al. (2015), the common feature among most models consists of an increase of clouds in the boundary layer and a larger (dominating) decrease of clouds in the free troposphere. The increase of boundary layer clouds has been linked to the shoaling and stabilization of the boundary layer and the decrease in cloud top entrainment (Kamae et al., 2015; Wyant et al., 2012; Xu et al., 2018). For the free troposphere, Kamae et al. (2015) correlate the decrease in cloud fraction to decreasing relative humidity (RH). Although tropospheric RH indeed decreases, the correlation between cloud fraction and RH does not necessarily indicate causality. Clouds and RH, as well as other variables of the hydrologic cycle, are expected to change in highly correlated ways, but the causality among them is not obvious.

Here, we seek to clarify the physical basis of the causal relationship between the CO_2 radiative forcing and cloud rapid adjustment. The availability of a physical basis and its consistency with GCM calculations would allow us to be more confident in the models. To this end, we begin by analyzing the experiments of the Atmospheric Model Intercomparison Project (AMIP, Cess & Potter, 1988; Taylor et al., 2012) and targeted GCM simulations that we carried out in aqua planet configuration (see section 2). Both the AMIP and aqua planet simulations project that during rapid adjustment (i) cloud water decreases in the free troposphere and (ii) the latitudinal profiles of the decreases of precipitation and cloud water path are highly correlated. The qualitative agreement between the AMIP and aqua planet simulations suggests that the land-sea contrast is not essential for rapid adjustment, a result consistent with Kamae and Watanabe (2013).

We therefore proceed to use the aqua planet simulations to test our hypothesis that the decreases in precipitation and cloud water are both consequences of the weakening of the moist diabatic circulation in the free troposphere, itself a result of the decrease in atmospheric radiative cooling due to increasing CO_2. The chain of causality—from the CO_2 radiative forcing to cloud rapid adjustment—is demonstrated in two steps. In step one (section 2), we argue that the decreases in precipitation and cloud water during rapid adjustment can be quantified by the decrease in the production of condensates in moist processes. The production of condensates takes place in the atmosphere via phase change of water (from vapor to condensates) as part of the hydrologic cycle. In step two (section 3), we show that the decrease in atmospheric radiative cooling due to increasing CO_2 weakens the moist diabatic circulation in the free troposphere, in which the production of condensates is reduced. By the result of step one, the weakening of the moist diabatic circulation is the cause for the decrease in cloud condensates in the free troposphere. The weakening of the circulation also explains the decrease in cloud fraction to a large extent. However, for this variable the RH change probably also plays a role. In section 4, we discuss the factors specific to the boundary layer that lead to the increase of clouds there. The paper ends with the conclusions in section 5.

2. Clouds, Precipitation, and Condensate Production

Our hypothesis is that the decreases in precipitation and in the mass of cloud condensates during rapid adjustment are governed by the same physics. In order to compare the latitudinal profiles of precipitation (P, kg $m^{-2}s^{-1}$) and condensate, we calculate the cloud water path (CWP, kg m^{-2}) by integrating the cloud (liquid and ice) water mixing ratio (q_c, kg kg^{-1}) over the atmospheric column. That is,

$$\frac{1}{g}\int_0^{p_s} q_c \mathrm{d}p = \mathrm{CWP} \tag{1}$$

assuming hydrostatic balance, where p is pressure, p_s is the surface pressure, and g is the gravitational acceleration.

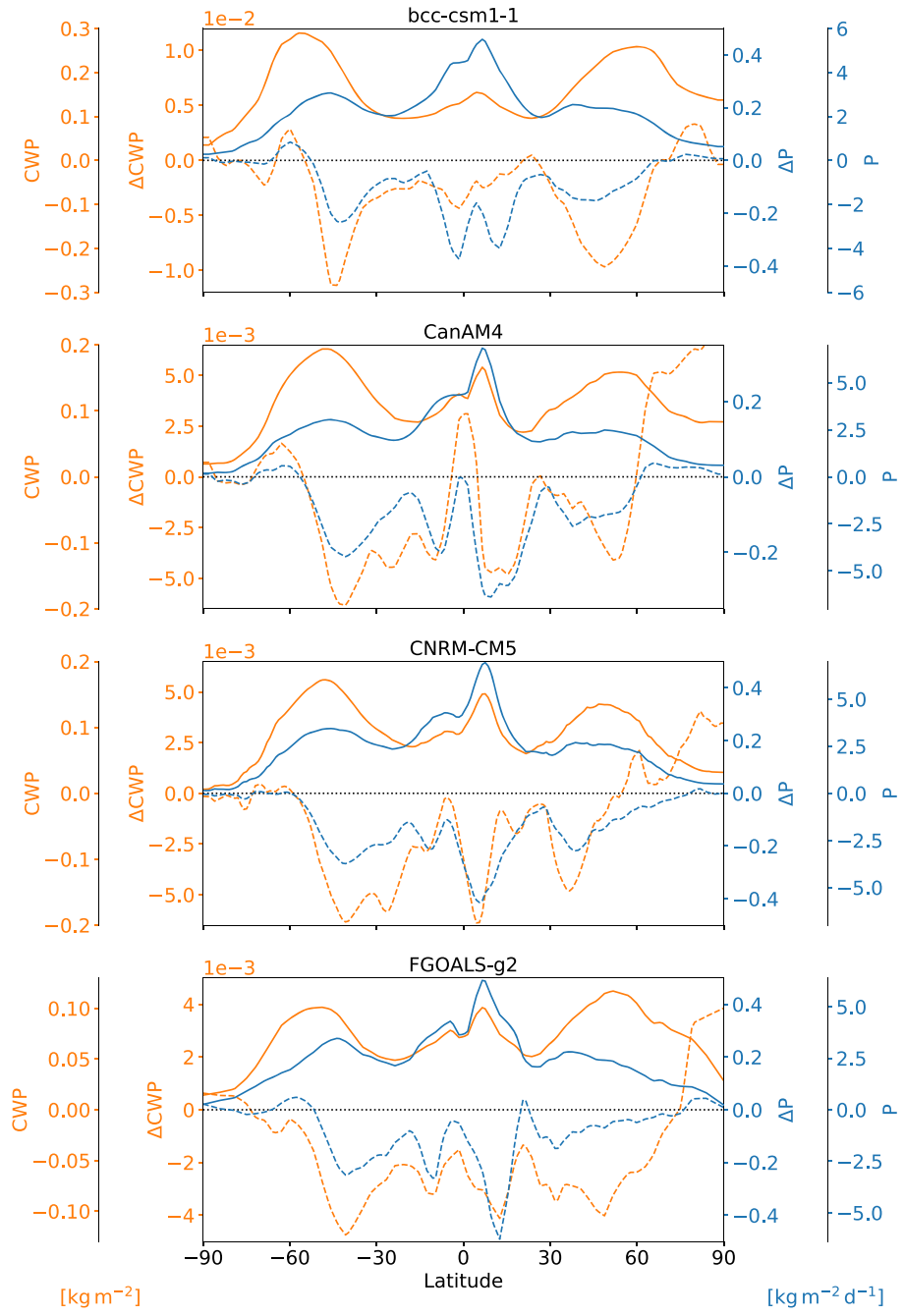

Figure 1. Latitudinal profiles of cloud water path (CWP) and precipitation (P) in the base state (solid) and the changes following rapid adjustment (dashed) diagnosed from the AMIP and AMIP4×CO_2 experiments produced by the bcc-csm1-1, CanAM4, CNRM-CM5, and FGOALS-g2 models.

Figures 1 and 2 show the results of the AMIP simulations by eight different GCMs (bcc-csm1-1, CanAM4, CNRM-CM5, FGOALS-g2, IPSL-CM5B-LR, MRI-CGCM3, MPI-ESM-MR, and MIROC5). The data of these simulations were downloaded from the Coupled Model Intercomparison Project Phase 5 (CMIP5) archive. The figures show that there is a strong correlation in the latitudinal profiles of precipitation (P) and cloud water path (CWP) in the base state (AMIP), as well as between their changes (ΔP and ΔCWP) following rapid adjustment (AMIP4×CO_2 minus AMIP). Further, the latitudinal profiles of ΔP and ΔCWP are approximately mirror images of precipitation in the base state. Specifically, the largest decreases in both precipitation and

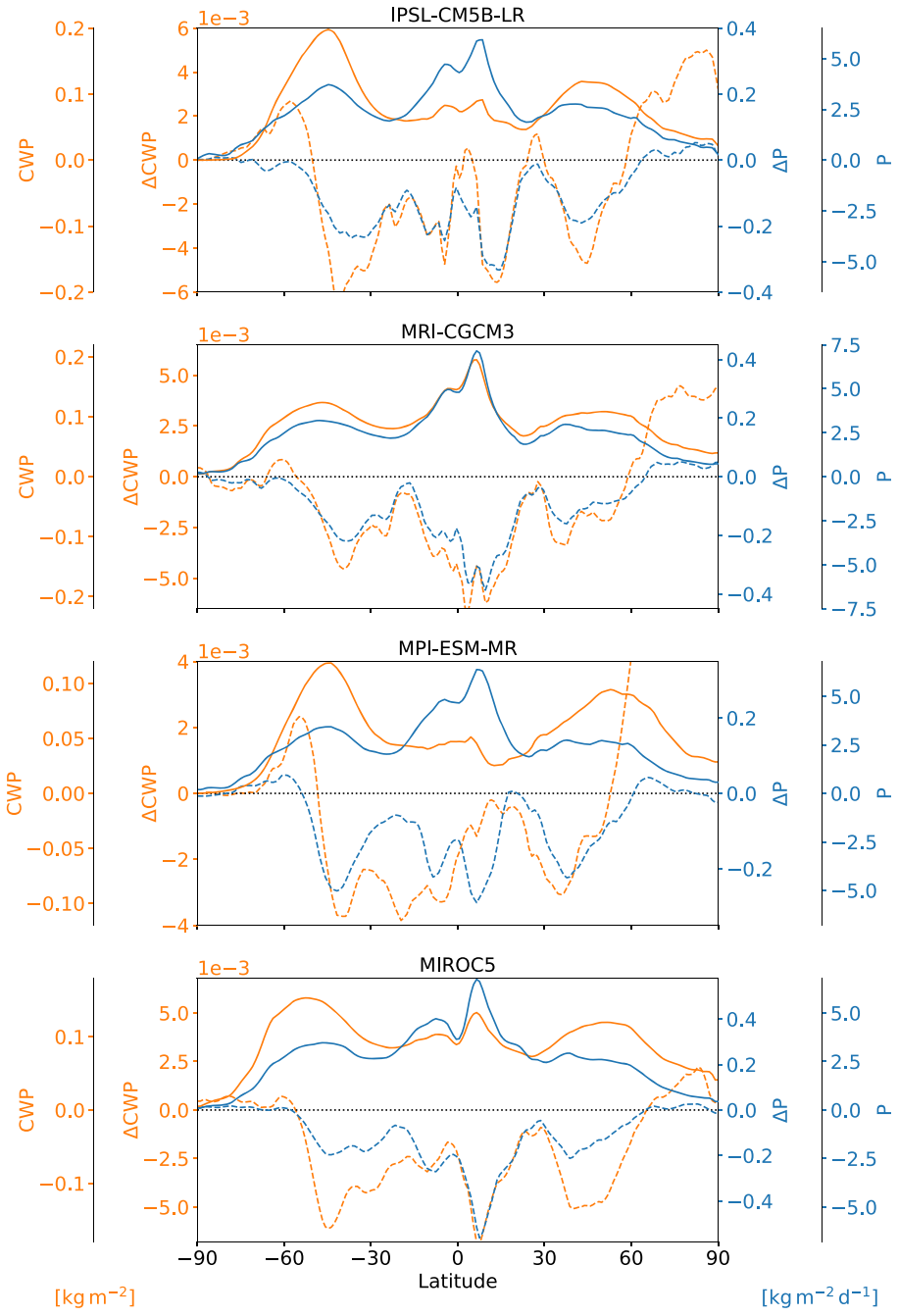

Figure 2. Same as Figure 1 but for the IPSL-CM5B-LR, MRI-CGCM3, MPI-ESM-MR, and MIROC5 models.

CWP occur at the Intertropical Convergence Zone (about 10° N) and in the mid-latitude storm tracks around 40°. These are well-known wet regions that receive the most amount of precipitation on Earth.

In addition to the AMIP experiments, we carried out simulations in aqua planet configuration using the HIgh Resolution Atmospheric Model (HiRAM, see Zhao et al., 2009). Three sets of aqua planet simulations were carried out, and these are labeled "CtrL" (control), "Cre0" (turning off cloud radiative effect, CRE), and "Ent0" (turning off subgrid-scale entrainment at cloud tops in the boundary layer). The purpose of these experiments is to show that the physical argument holds regardless of CRE and the parameterization of subgrid-scale entrainment, which we expect to be highly model specific. Other technical details of HiRAM and the simulations are provided in Appendix A.

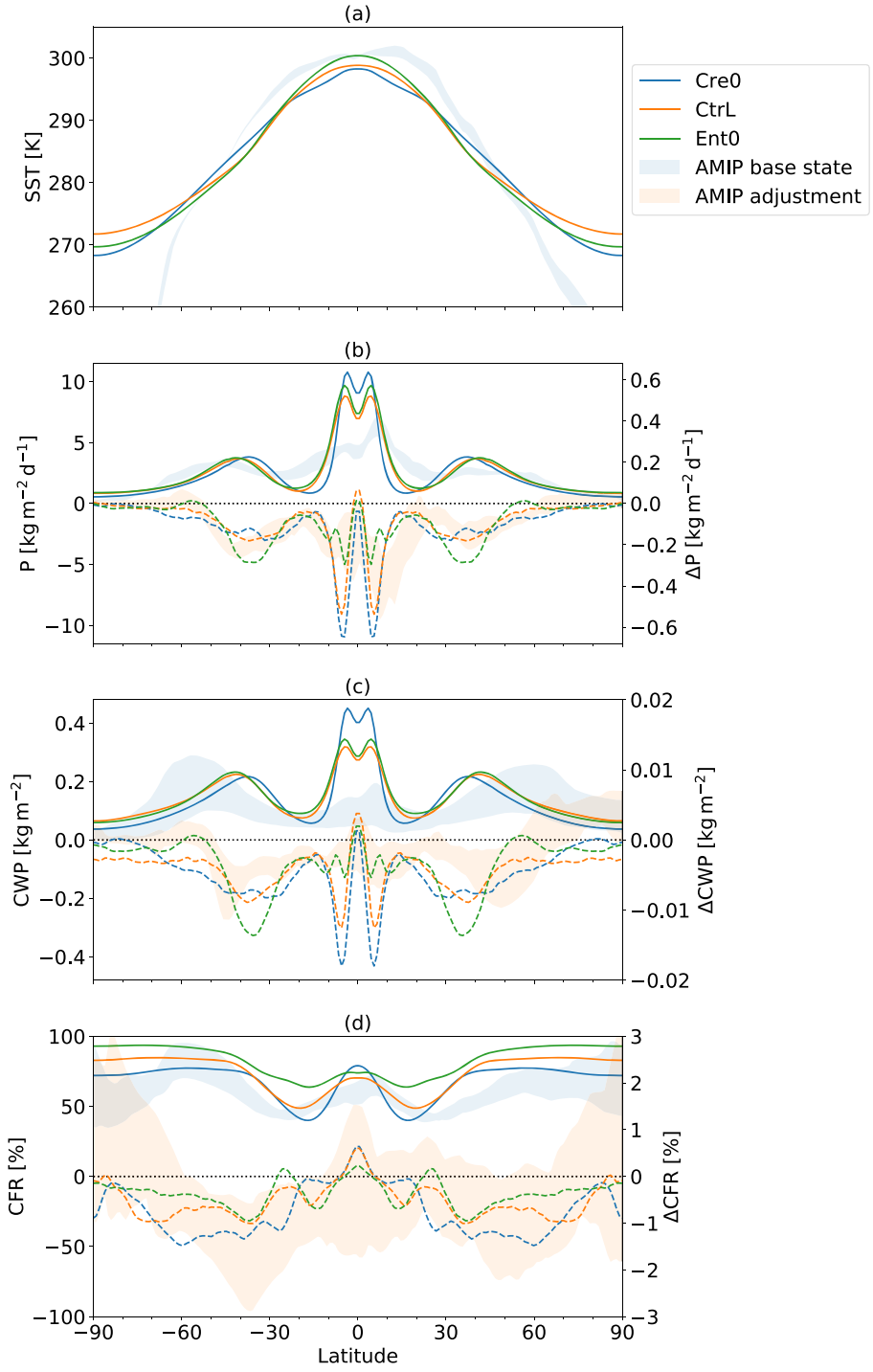

Figure 3. Latitudinal profiles of (a) surface temperatures, (b) precipitation, (c) CWP, and (d) total CFR in the base state (solid) and their rapid adjustments under 4×CO_2 (dashed) in the HiRAM aqua planet simulations and the AMIP experiments (shaded).

The latitudinal profiles of surface temperatures, precipitation, CWP, and total cloud fraction (CFR) in both the AMIP and aqua planet simulations are shown in Figure 3. The shaded areas in Figure 3 show the range of the AMIP data of the eight CMIP5 models. The meridional gradient of the sea surface temperatures in the tropics is smaller in the AMIP experiments than in the aqua planet simulations. Correspondingly, the tropical precipitation maximum is smaller, and the tropical precipitation pattern is wider in the AMIP experiments than in the aqua planet simulations. In both the AMIP and aqua planet simulations, the changes in

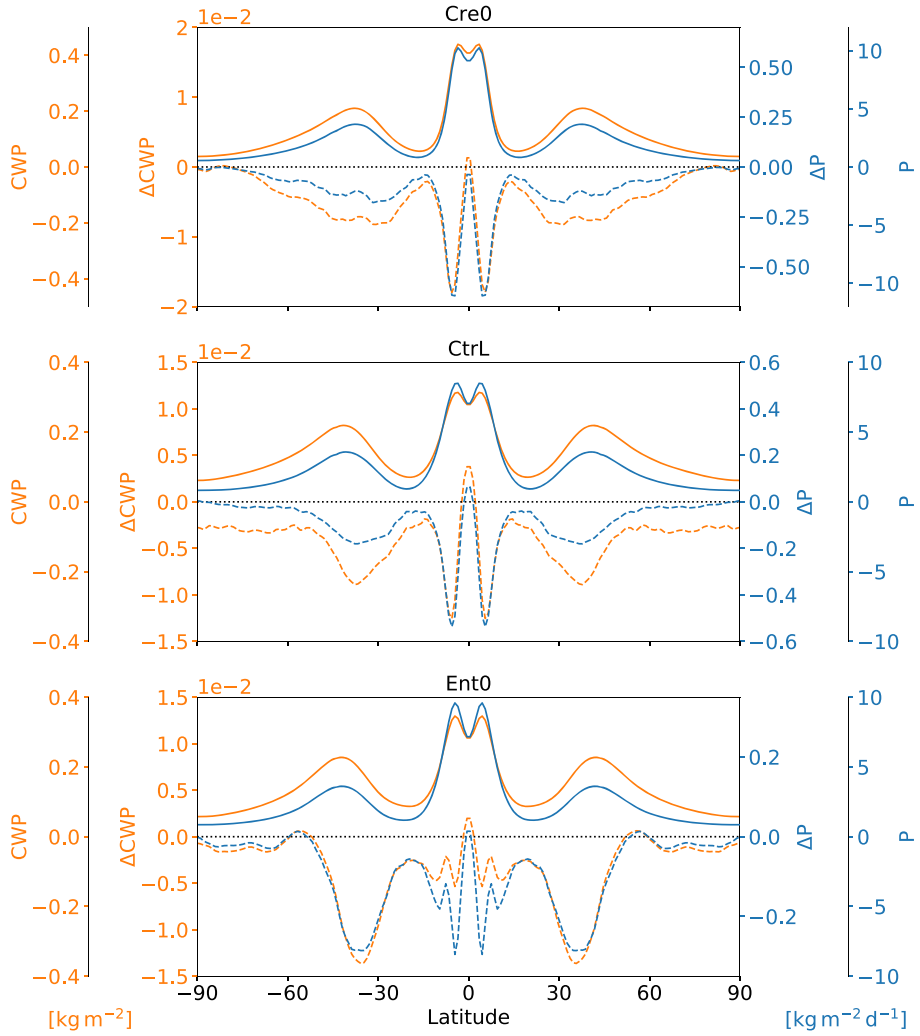

Figure 4. Latitudinal profiles of CWP and precipitation (P) in the base state (solid) and the changes following rapid adjustment under 4×CO_2 (dashed) in the HiRAM aqua planet simulations.

precipitation and CWP following rapid adjustment are approximately reflections of their base state profiles, except for the fact that the maximum decreases in precipitation and CWP in the mid-latitudes are located slightly equatorward of the maximum precipitation and CWP in the base state.

Figure 3 shows that the latitudinal profiles of precipitation and CWP are highly correlated in both the base state and in the changes following rapid adjustment. The latitudinal profiles of precipitation and CWP in the three aqua planet simulations are also shown in Figure 4, which can be compared with the AMIP experiments shown in Figures 1 and 2. The figures show that the land-sea contrast regulates the latitudinal profiles of precipitation and clouds, but it is clear that the correlation between the two variables, precipitation and CWP, holds well in both the aqua planet and AMIP experiments across all models. A high correlation between precipitation and CWP is not guaranteed a priori because (i) some cloud condensates evaporate in the air and therefore do not fall to the surface as precipitation and (ii) the fall speeds of the condensates affect the rate of precipitation. The empirical correlation between precipitation and CWP changes indicates that, at least so far as rapid adjustment is calculated in these GCMs, the changes in condensate evaporation and sedimentation are only secondary.

Figure 3 shows that the CFR is however somewhat decoupled from precipitation and CWP. In the high-latitudes poleward of 60°, there is large cloud cover especially in the aqua planet simulations (more than 70%), but these clouds are optically thin (low water content) and are non-precipitating. In the mid-latitudes, the regions that exhibit reduction in CFR during rapid adjustment ($\Delta CFR < 0$) are located

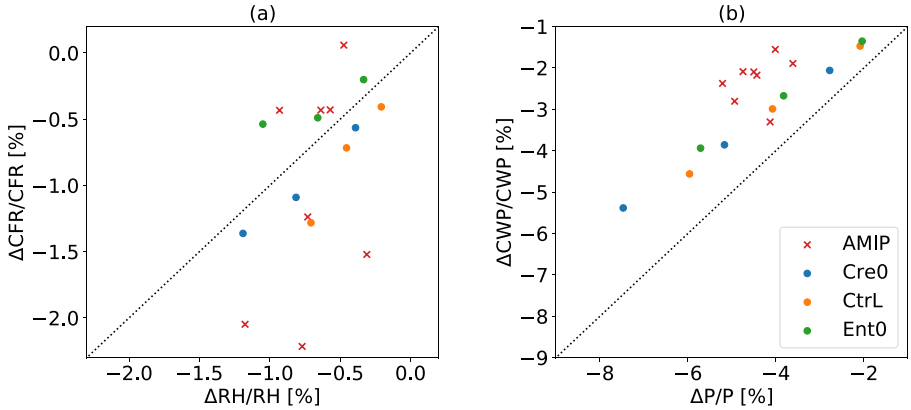

Figure 5. Percentage changes associated with rapid adjustment of the global average (a) CFR and tropospheric RH (below 150 hPa) and (b) CWP and precipitation. The crosses show the difference between the AMIP and AMIP4×CO_2 experiments. The circles show the data of the HiRAM simulations (labeled Cre0, CtrL, and Ent0) with doubled (2×), quadrupled (4×), and octupled (8×) CO_2 concentrations. The dotted lines are the one-to-one lines.

poleward of the regions that exhibit reduction in CWP. The magnitude of ΔCFR is smaller in the deep tropics than in the mid-latitudes, while the magnitude of ΔCWP in the deep tropics is comparable or larger than in the mid-latitudes. We expect that CFR is highly sensitive to the identification of "cloudy area" and parameterization of entrainment (which controls the mixing between cloudy and surrounding air) in models. Indeed, Figure 3d shows large variations in ΔCFR among the CMIP5 models.

The decrease in tropospheric RH has been proposed to be the mechanism for the decrease in CFR during rapid adjustment (Kamae & Watanabe, 2012; Kamae et al., 2015). We therefore examine whether ΔRH is a good predictor for ΔCFR. Suppose that in the base state CFR correlates with tropospheric RH (below 150 hPa) such that we can write CFR ∝ RH. If ΔRH is the dominating factor governing ΔCFR, we may linearize the fractional changes of CFR and RH as

$$\frac{\Delta \mathrm{CFR}}{\mathrm{CFR}} \sim \frac{\Delta \mathrm{RH}}{\mathrm{RH}}. \tag{2}$$

In other words, if ΔRH is the dominating factor governing ΔCFR, we expect to see a one-to-one relationship between ΔCFR/CFR and ΔRH/RH. Figure 5a shows however that this is not the case. Across the eight CMIP5 models the range of ΔCFR/CFR is significantly larger than the range of ΔRH/RH.

On the other hand, our argument is that the decrease in the mass of cloud condensates is governed by the same physics that leads to the decrease in precipitation. By a similar scaling argument as in equation (2), we expect that

$$\frac{\Delta \mathrm{CWP}}{\mathrm{CWP}} \sim \frac{\Delta \mathrm{P}}{\mathrm{P}}. \tag{3}$$

Figure 5b confirms that ΔCWP indeed scales with ΔP to first order. The deviation between the aqua planet data and the one-to-one line can be attributed to the increase of low clouds in the boundary layer (see Figure 6). Note that the quantity ΔCWP measures the change in the mass of cloud condensates over the entire atmospheric column (without accounting for the different behavior of clouds in the boundary layer). The AMIP data show further deviation from the one-to-one line, indicating some complications due to land-sea contrast. In general, the decrease in CWP is smaller in the AMIP experiments than in the aqua planet simulations. Kamae and Watanabe (2013) showed that land surface warming induces anomalous upward motion, which increases high clouds over lands. The land-induced adjustment thus counteracts the decrease of clouds over oceans. Also, there could be a shift of clouds from oceans to lands in the AMIP experiments, as suggested by Wyant et al. (2012) and Xu et al. (2018). The land-sea contrast thus quantitatively affects the results, but it is not a necessary requirement for rapid adjustment (Kamae & Watanabe, 2013).

The results thus far show that precipitation and the mass of cloud condensates are highly correlated variables of the hydrologic cycle. We reason that these two variables are controlled by the same process, which is the production of condensates via phase change of water (from vapor to condensates) in the atmosphere as part

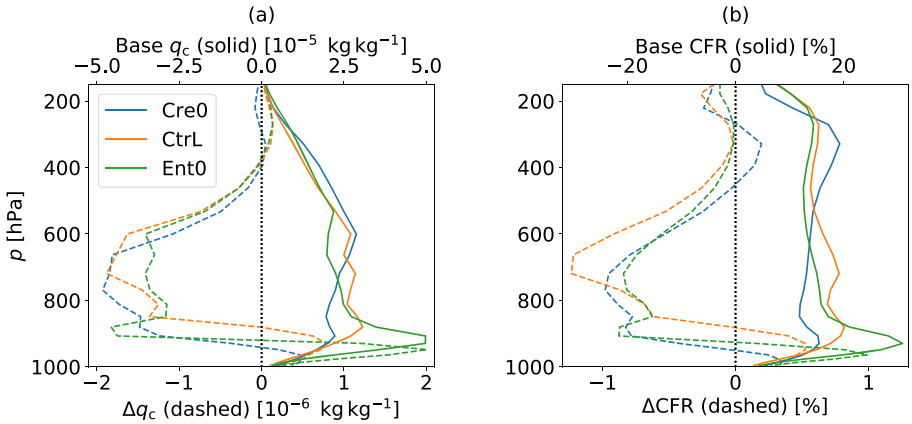

Figure 6. Vertical profiles of the global average (a) cloud water mixing ratio q_c and (b) cloud fraction (CFR) in the base state (solid) and the changes following rapid adjustment under 4×CO_2 (dashed) in the HiRAM aqua planet simulations.

of the hydrologic cycle. The variable required for the diagnosis of phase change in moist processes in models is the tendency (rate of change) of the mixing ratio of the condensates that arises from phase change, which we denote by m_{cond} (in units of kg kg^{-1} s^{-1}). The sign convention of m_{cond} is that where m_{cond} is positive, condensation takes place. Vice versa, where m_{cond} is negative, evaporation of the condensates occurs. The integral over the atmosphere of m_{cond} is positive because the overwhelming direction of phase change in the atmosphere is from water vapor to condensates. Assuming hydrostatic balance, we have confirmed that in HiRAM the vertical integral of m_{cond} gives precipitation P, that is

$$\frac{1}{g}\int_0^{p_s} m_{\text{cond}}\mathrm{d}p = \mathrm{P}. \tag{4}$$

Unfortunately m_{cond} is not available as an output of the other CMIP5 models, and so hereafter, we focus on the analyses of the HiRAM simulations only.

Figure 7 shows that in the HiRAM simulations Δq_c and Δm_{cond} are highly correlated, particularly in the latitudinal direction. The cloud mixing ratio is reduced ($\Delta q_c < 0$) in the latitudes in which $\Delta m_{\text{cond}} < 0$. Because the vertical integral of q_c gives CWP (equation (1)) and the vertical integral of m_{cond} gives precipitation (equation (4)), we have correspondingly $\Delta\text{CWP} < 0$ in the latitudes in which $\Delta\text{P} < 0$ (Figure 4). In the vertical direction, however, the profile of Δq_c is shifted slightly upward relative to the profile of Δm_{cond} (see the regions around 700 hPa and 30°–40° in Figure 7). This vertical displacement between q_c and m_{cond} is also apparent in the base state (not shown). In regions where $q_c > 0$ but a significant amount of cloud water evaporates in situ, the magnitude of the net rate of condensate production m_{cond} (which is actually the sum of condensate production and condensate evaporation) is small.

Figure 7 shows that the total rapid adjustment consists of a decrease of clouds (correspondingly $\Delta m_{\text{cond}} < 0$) above about 900 hPa and an increase of clouds (correspondingly $\Delta m_{\text{cond}} > 0$) below this level. In the vertical, cloud changes are consistent between the global average Δq_c and ΔCFR (Figure 6) despite the differences in their latitudinal profiles shown earlier in Figure 3. Clouds in the transition layer between 800 and 900 hPa are influenced by both the free tropospheric circulation and the physical processes of the boundary layer. Below, we discuss separately the role of the free tropospheric circulation in section 3 and other processes affecting clouds in the boundary layer in section 4.

3. Circulation Governs Condensate Production in the Free Troposphere

The physical argument in this section is based on the energetic balance between radiative cooling and latent heat released in moist processes in the free troposphere (see, e.g., Betts & Ridgway, 1988; Allen & Ingram, 2002; Mitchell et al., 1987; O'Gorman et al., 2012; Pendergrass & Hartmann, 2014, among others). Below, we write down the mathematical basis of the energetic balance, which allows us to formally define the metric measuring the strength of the moist diabatic circulation in the free troposphere and relate it to the rate of condensate production (m_{cond}) introduced earlier in section 2.

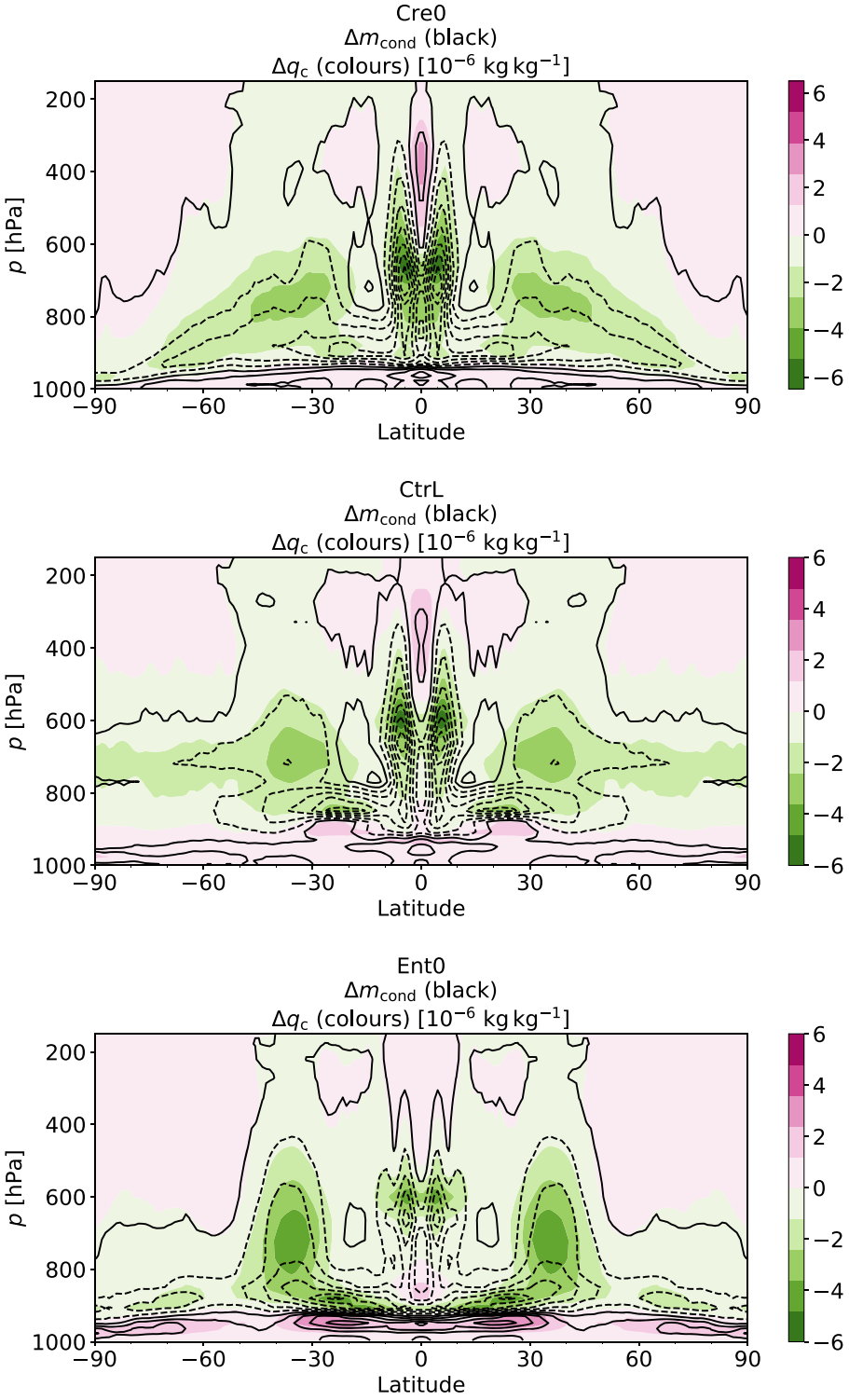

Figure 7. Spatial structures of Δm_{cond} (black contours) and Δq_c (filled colored contours) following rapid adjustment under 4×CO_2 in the Cre0 (top), CtrL (middle), and Ent0 (bottom) simulations.

The thermodynamic energy equation in pressure coordinates is given by

$$\frac{\partial T}{\partial t} + \vec{v} \cdot \nabla T - \omega\sigma = Q_{\text{rad}} + Q_{\text{lat}} + Q_{\text{sens}} \tag{5}$$

(cf. Equation 7 in Dinh & Fueglistaler, 2017). Here T is temperature, $\vec{v}$ is the horizontal wind field, σ is the static stability, ω is the pressure velocity, Q_{rad} is the radiative heating rate, Q_{lat} is the latent heating rate, and Q_{sens} is the atmospheric temperature tendency that results from the vertical diffusion of sensible heat flux by the boundary layer schemes in GCMs. In the base state the atmosphere is dominated by radiative cooling ($Q_{\text{rad}} < 0$). As CO_2 concentration increases, absorption of longwave radiation by the atmosphere increases, and so the radiative heating rate increases. As the radiative heating rate increases ($\Delta Q_{\text{rad}} > 0$) and equivalently atmospheric radiative cooling decreases, latent and sensible heat decrease ($\Delta Q_{\text{lat}} < 0$ and $\Delta Q_{\text{sens}} < 0$).

As a metric for the strength of the moist diabatic circulation regulated by the "diabatic" heating rates on the right hand side of equation (5), we use the radiative subsidence mass flux defined by

$$\omega_{\text{rad}} \equiv -\frac{Q_{\text{rad}}}{\sigma}. \tag{6}$$

The static stability σ is calculated as

$$\sigma = \frac{RT}{pc_p} - \frac{\partial T}{\partial p},$$

where R is the specific gas constant of air and c_p is the specific heat at constant pressure of air. The sign convention for ω_{rad} is that it is positive (indicating subsidence) in the base state. This method (equation (6)) to estimate the subsidence air mass flux within the moist diabatic circulation was also used by Yano et al. (2002), Folkins et al. (2008), Zelinka and Hartmann (2010), and Dinh and Fueglistaler (2017). The change in the radiative heating rate (ΔQ_{rad}) and the change in the radiative subsidence ($\Delta\omega_{\text{rad}}$, calculated based on equation (6)) are shown in Figure 8a. The similarity in the vertical profiles of these two variables shows that for the most part the decrease in the subsidence max flux ($\Delta\omega_{\text{rad}} < 0$) is forced directly by the decrease in atmospheric radiative cooling ($\Delta Q_{\text{rad}} > 0$), rather than from the change in the static stability.

In the free troposphere above about 800 hPa, Q_{sens} is negligible (see Figure 2 in Dinh & Fueglistaler, 2017), and so the moist diabatic circulation can be theoretically constructed as consisting of a subsidence branch associated with Q_{rad} and an ascending branch associated with Q_{lat}. Mass conservation implies that, on the global average, the radiative subsidence estimated by ω_{rad} is balanced by the rising motions driven by the latent heat released in moist processes, that is

$$[\omega_{\text{rad}}] = -[\omega_{\text{lat}}]. \tag{7}$$

The equality holds only at steady state and for a closed circulation, that is, on the global average as indicated by the brackets $[\cdot]$. Because equation (7) holds only at steady state, one may pose the question as to how the ascending air within the convective regions initially "knows" that it needs to slow down to adjust to the CO_2 radiative forcing. The stratification at the top of the boundary layer's inversion is particularly important in determining the ascending air mass flux into the free troposphere. The increase in the radiative heating rate ($\Delta Q_{\text{rad}} > 0$) induces tropospheric warming with a maximum at around 800 hPa (Figure 8b), which increases the static stability in the critical layer at the top of the boundary layer at 800 hPa and therefore throttles and weakens the ascending motions into the free troposphere.

The rate of condensate production in the ascending regions can be estimated by

$$-[\omega_{\text{lat}}]\left[\frac{\mathrm{d}q_{\text{sat}}}{\mathrm{d}p}\right] = [\omega_{\text{rad}}]\left[\frac{\mathrm{d}q_{\text{sat}}}{\mathrm{d}p}\right] \equiv m_{\text{rad}}, \tag{8}$$

where q_{sat} is the saturation specific humidity (see also Dinh & Fueglistaler, 2017; O'Gorman & Schneider, 2009; Schneider et al., 2010). There is non-negligible error in the estimate in equation (8) because q_{sat} within the ascending regions may not be equal to the global average q_{sat}. Nevertheless, we have shown in Dinh and Fueglistaler (2017) that m_{rad} is a relatively good metric for m_{cond} in the free troposphere. The approximate agreement between m_{cond} and m_{rad} indicates that the evaporation of the condensates in the air—which contributes to the net condensate production m_{cond} but is not accounted for in m_{rad}—can be neglected to first

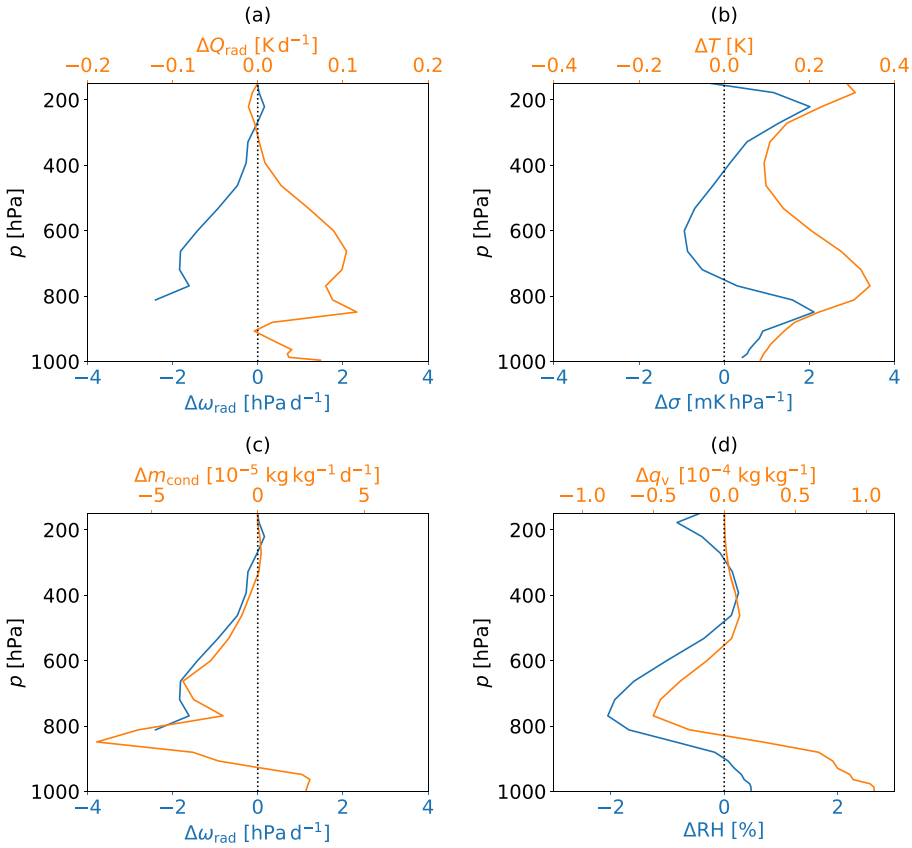

Figure 8. Vertical profiles of the global average (a) ΔQ_{rad} and $\Delta\omega_{rad}$, (b) ΔT and $\Delta\sigma$, (c) Δm_{cond} and $\Delta\omega_{rad}$, and (d) Δq_v and ΔRH under 4×CO_2 in the CtrL case. The results of the Cre0 and Ent0 cases are qualitatively similar (not shown). The radiative subsidence ω_{rad} is shown above 800 hPa only.

order. Note that the variable m_{cond} is diagnosed directly from the model output, and here we are linking it to the metric m_{rad}, which is defined based on Q_{rad} (see equations (6) and (8)). In the boundary layer, sensible heat plays a key role in balancing Q_{rad}, and ascending air may not be at saturation (see Betts & Ridgway, 1988; Dinh & Fueglistaler, 2017; Mitchell et al., 1987; Takahashi, 2009). Therefore, ω_{rad} (equation (6)) and m_{rad} (equation (8)) are useful only in the free troposphere above 800 hPa.

Because the temperature adjustment is small ($\Delta T \sim 0.2$K for 4×CO_2, see Figure 8b), the contribution of Δq_{sat} to Δm_{rad} can be neglected. Quantitatively, the percentage change of q_{sat} is on the order of 1%, and the percentage change of ω_{rad} is on the order of −5% for 4×CO_2. Therefore, we expect that to first-order Δm_{rad} and so Δm_{cond} scale with $\Delta\omega_{rad}$. Figure 8c confirms that $\Delta\omega_{rad}$ is indeed a good predictor for Δm_{cond}. Results in section 2 have shown that the decrease in the rate of condensate production ($\Delta m_{cond} < 0$) explains the decrease in the mass of cloud condensates ($\Delta q_c < 0$). Based on these, we conclude that the weakening of the moist diabatic circulation (as measured by $\Delta\omega_{rad} < 0$) in the free troposphere is the reason for the decrease in the production of condensates and therefore also the decrease in the mass of cloud condensates there.

Finally, we revisit the scaling argument analogous to equation (3), but now we apply it to the free troposphere above 800 hPa only. Figure 9a shows that Δm_{cond} is the dominating factor governing Δq_c. For the free troposphere we can therefore write

$$\frac{\Delta q_c}{q_c} \sim \frac{\Delta m_{cond}}{m_{cond}},$$

but

$$\frac{\Delta m_{cond}}{m_{cond}} \sim \frac{\Delta \omega_{rad}}{\omega_{rad}}$$

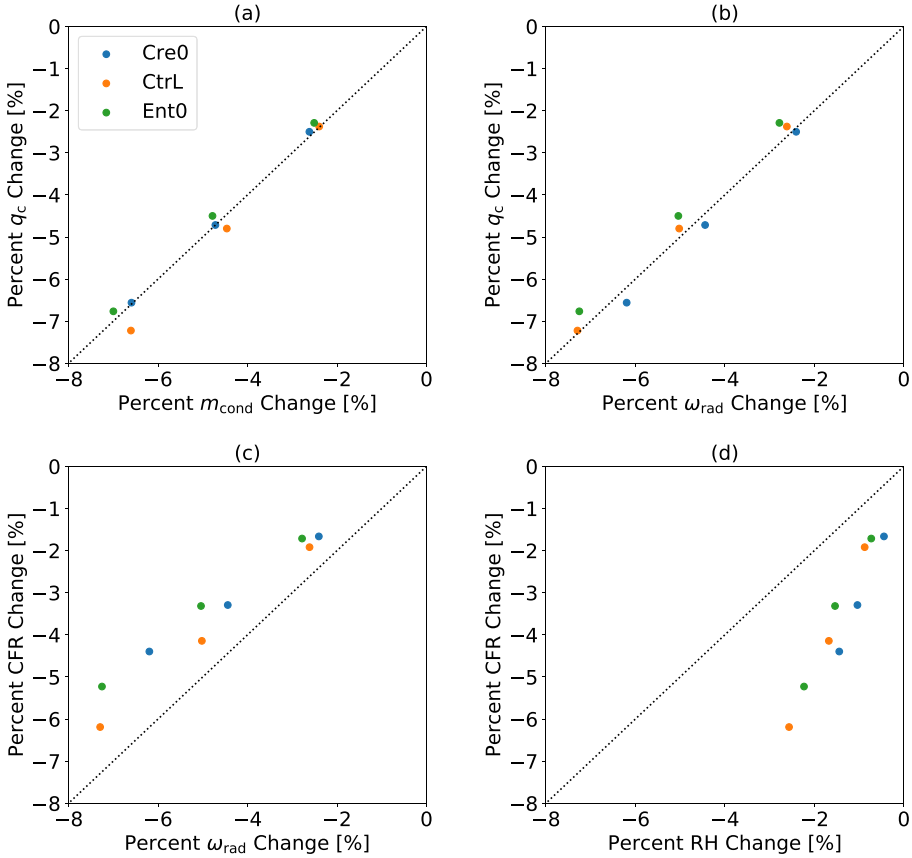

Figure 9. Percentage changes associated with rapid adjustment of the global average (a) q_c versus m_{cond}, (b) q_c versus ω_{rad}, (c) CFR versus ω_{rad}, and (d) CFR versus RH. Each HiRAM configuration (labeled Cre0, CtrL, and Ent0) has three data points corresponding to doubled (2×), quadrupled (4×), and octupled (8×) CO_2 concentrations. All variables shown have been pressure-weighted averaged for the free troposphere between 800 and 150 hPa. The dotted lines are the one-to-one lines.

based on the relationship between the circulation and the rate of condensate production demonstrated above (recall Figure 8c). Therefore,

$$\frac{\Delta q_c}{q_c} \sim \frac{\Delta \omega_{rad}}{\omega_{rad}}$$

as confirmed in Figure 9b. The weakening of the circulation also explains the decrease in CFR to a large extent (Figure 9c), but for this variable RH may also play a secondary role (Figure 9d).

4. Clouds in the Boundary Layer

Figure 6 shows that clouds (in terms of both q_c and CFR) decrease in the free troposphere but increase below about 900 hPa in the HiRAM aqua planet simulations. The upper half of the boundary layer between 800 and 900 hPa shows a decrease in clouds, which is consistent with the weakening of the circulation in the free troposphere, but clouds in this layer are also influenced by physical processes of the boundary layer. It has been suggested that the stabilization and shoaling of the boundary layer and the decrease in turbulent entrainment at cloud tops are factors contributing to cloud rapid adjustment in the boundary layer below 800 hPa (Kamae et al., 2015; Wyant et al., 2012; Xu et al., 2018).

It can be argued that turbulent entrainment is simulated well only in high-resolution models such as the superparameterized GCMs used by Wyant et al. (2012) and Xu et al. (2018). Superparameterized GCMs are coupled with sophisticated cloud-resolving and/or high-order turbulent closure schemes. However, even in these models the response of clouds to entrainment is highly sensitive to model resolution and the details of the cloud and turbulent schemes, such that the model used by Wyant et al. (2012) shows relatively little

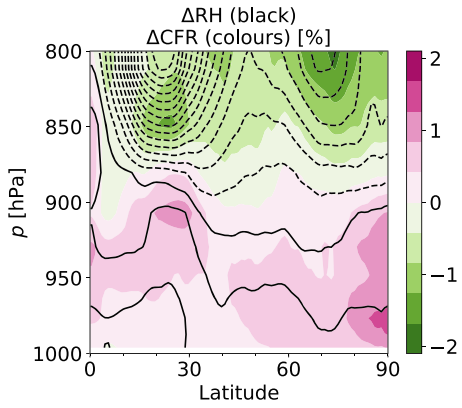

Figure 10. Spatial structures of ΔRH and ΔCFR in the boundary layer in the CtrL case. The results of the Cre0 and Ent0 cases are qualitatively similar (not shown). The solid black contours show the non-negative (zero and above) values of ΔRH. The dashed black contours show the negative values of ΔRH.

change in low clouds, while the one used by Xu et al. (2018) shows a significant increase (which is consistent with the HiRAM results). Large eddy simulations at very high resolutions have also been used to study cloud rapid adjustment (e.g., Blossey et al., 2016). However, the limitation of these limited-domain large eddy simulations is that they cannot account for the global energetic equilibration following the increase in CO_2 and the resulting adjustment of the global tropospheric circulation and hydrologic cycle.

Given the known sensitivity of low clouds to model configurations, we investigate the role of parameterized subgrid-scale entrainment in HiRAM in the Ent0 experiments. With subgrid-scale entrainment at cloud tops turned off, the Ent0 case produces the largest amount of clouds in the base state (Figure 3d), specifically at around 900 hPa (Figure 6). The increase in boundary layer clouds during rapid adjustment is also largest in the Ent0 case (Figure 8a). This large increase in clouds appears unrelated to entrainment change because the Ent0 case has the least amount of entrainment and hence the least decrease in entrainment. Rather, we interpret the large increase in boundary layer clouds in the Ent0 case as a reflection of the large amount of clouds in the base state in this case.

A factor that has not been discussed previously in consideration of cloud rapid adjustment in the boundary layer is the change in near-surface RH. Kamae and Watanabe (2012, 2013) reported that near-surface RH increases following rapid adjustment in GCMs. However, the authors did not consider this as a factor regulating cloud rapid adjustment in the boundary layer. Their schematics explaining cloud rapid adjustment (Figure 16 in Kamae & Watanabe, 2013 and Figure 1 in the subsequent review paper Kamae et al., 2015) neglect that RH increases near the surface and depict instead that RH decreases throughout the whole troposphere.

Figure 8d shows that RH increases near the surface in HiRAM. This behavior is consistent with Kamae and Watanabe (2012, 2013) and also with Xu et al. (2018). We show further here (see Figure 10) that the spatial structures of ΔRH and ΔCFR in the boundary layer are highly correlated. Both ΔRH and ΔCFR switch signs from negative above about 900 hPa to positive below this level. The 900 hPa level is approximately the lifting condensation level (LCL, see O'Gorman et al., 2012; Takahashi, 2009). Below the LCL, the presence of clouds is largely controlled not by the formation of the condensates but by the evaporation of the condensates as they fall through the air. We therefore expect that below the LCL, large RH (moist air) favors large cloud amount. Due to gravitational settling of the condensate particles, the zero contour of ΔCFR is located slightly below the zero contour of ΔRH.

It is interesting to address the question why RH increases near the surface. Such an increase in RH cannot be explained from the temperature change because $\Delta T > 0$ throughout the troposphere (see Figure 8b). Figure 8d shows that RH increases near the surface due to an increase in the specific humidity (q_v) near the surface. Part of the effect of $\Delta q_v > 0$ which increases RH is canceled out by the effect of $\Delta T > 0$ which decreases RH. Therefore, the layer in which RH increases is shallower than the layer in which q_v increases. In Dinh and Fueglistaler (2017), we have shown that the specific humidity near the surface increases because the demand for near-surface moisture to be exported to the free troposphere decreases as the moist diabatic circulation in the free troposphere weakens. The increase in near-surface specific humidity is the precondition for the decrease of surface evaporation during rapid adjustment.

5. Conclusions

The AMIP and aqua planet experiments provided a set of global climate simulations with varied regional patterns in the atmospheric general circulation and hydrologic cycle. Despite the differences in the circulation patterns in these simulations, the correlation between precipitation and CWP always holds well. Precipitation and cloud condensates are connected by the phase change processes that convert water vapor to condensates in the atmosphere as part of the hydrologic cycle. However, a correlation between condensate production and cloud condensates is not guaranteed a priori because condensation governs cloud formation but not subsequent cloud evolution. Therefore, the finding of a high correlation between precipitation and

the mass of cloud condensates indicates that the decrease in condensate production is the dominating effect leading to the decrease of cloud condensates during rapid adjustment, while other changes in subsequent cloud evolution are secondary factors.

We have explained the decrease in condensate production as a result of the weakening of the moist diabatic circulation in the free troposphere. The strength of the moist diabatic circulation is quantified by the radiative subsidence mass flux, which is calculated by the radiative heating rate divided by the stratification (see equation (6)). Following CO_2 increase, tropospheric radiative cooling is reduced, which induces tropospheric temperature adjustment with a maximum warming at about 800 hPa (top of the boundary layer). The decrease in radiative cooling (rather than stratification change) is the dominating effect that accounts for the decrease in the radiative subsidence mass flux. On the other hand, the stabilization of the inversion layer at the top of the boundary layer that arises from the temperature adjustment is critical in the slow down of the ascending branch of the circulation. Via the relationships between clouds and condensate production, condensate production and circulation, and circulation and atmospheric radiation, we have demonstrated how the CO_2 radiative forcing forces cloud rapid adjustment in the free troposphere.

In the boundary layer, clouds increase (instead of decrease like in the free troposphere) during rapid adjustment in most GCMs (Kamae et al., 2015) including HiRAM (as shown in this work). The increase in boundary layer clouds has been previously discussed in association with the shoaling and stabilization of the boundary layer and the decrease in cloud top turbulent entrainment (Kamae et al., 2015; Wyant et al., 2012; Xu et al., 2018). Additionally, we suggest that the increase in RH below the LCL (approximately 900 hPa) contributes to the increase of clouds there. Clouds below the LCL are governed by the evaporation of the condensates as they fall through the air, such that large RH favors more clouds. RH increases below the LCL because the specific humidity increases there. In Dinh and Fueglistaler (2017), we have shown that the specific humidity near the surface increases because the demand for near-surface moisture to be exported to the free troposphere decreases as the moist diabatic circulation in the free troposphere weakens.

Appendix A: Method

We carried out simulations of rapid adjustment using HiRAM, a GCM developed by the Geophysical Fluid Dynamics Laboratory (GFDL). In order to test the cloud response over a wide range of forcing, we performed the simulations with doubled (2×), quadrupled (4×), and octupled (8×) CO_2 concentrations. The AMIP data are available for the quadrupling CO_2 scenario only. Furthermore, the rate of condensate production (m_{cond}) is not available as an output in the AMIP data, but we are able to print it out for HiRAM. We used a C90 grid (Harris & Lin, 2014) of 1° horizontal resolution and 32 vertical levels in the atmosphere.

The HiRAM simulations were run in aqua planet configuration in which ice formation at the surface is suppressed. The aqua planet simulations together with the AMIP experiments allow us to demonstrate that the relationship between precipitation and cloud water holds regardless of land and ice surfaces (see Figures 1–5). We do not compare in detail the aqua planet and AMIP experiments to quantify the role of land-sea contrast, as this topic has been thoroughly addressed elsewhere (see, e.g., Chung & Soden, 2018; Kamae & Watanabe, 2013; Medeiros et al., 2015; Ringer et al., 2014).

Rapid adjustment has been diagnosed in both transient climate simulations using coupled atmosphere-ocean GCMs (Andrews & Forster, 2008; Andrews et al., 2012; Gregory & Webb, 2008; Gregory et al., 2004; Zelinka et al., 2013) and prescribed-surface simulations using atmosphere-only GCMs (Bala et al., 2009; Hansen, 2002; Hansen et al., 2005; Kamae & Watanabe, 2012; Shine et al., 2003; Vial et al., 2013; Zelinka et al., 2013). Given that our focus is to quantify the changes in the atmosphere following rapid adjustment (rather than to realistically simulate the time scale of transient climate changes), we opted for the prescribed-surface method to avoid the error associated with regression which is necessary to diagnose rapid adjustment in transient climate simulations.

To obtain the sea surface temperatures (SSTs) required as the lower boundary condition for our simulations, we used HiRAM to run aqua planet simulations in which the atmosphere is coupled to a slab ocean. In these coupled slab-ocean simulations, atmospheric CO_2 is prescribed to be 400 ppmv, and a uniform surface albedo is chosen such that in equilibrium, the global average surface temperature is 288 K, which is representative of the current Earth's climate. The equilibrium SSTs obtained from the slab-ocean simulations are then imposed as the lower boundary condition in the prescribed-surface simulations (AMIP-type

runs). For each of the profiles of SSTs that has been obtained from the coupled slab-ocean simulations, we ran four prescribed-surface simulations with 100, 200, 400, and 800 ppmv CO_2. Thus, the SSTs and also the surface albedo are fixed while CO_2 is varied among these four runs. Rapid adjustment under doubled (2×), quadrupled (4×), or octupled (8×) CO_2 is diagnosed as the difference between the 400, 200, or 100 ppmv runs, respectively, and the 800 ppmv CO_2 run. All results discussed are based on the 11-year averages of the model solutions after an equilibrated (steady) state has been reached.

Note that the splitting of the precipitation patterns at the equator in the HiRAM simulations (Figure 3b) is not strictly a double Intertropical Convergence Zone but an effect of time averaging over the 11-year model output. The precipitation patterns have no double peaks in the tropics in any given month and a single tropical precipitation maximum moves between the Northern and Southern Hemispheres as insolation varies seasonally (not shown).

To explore the sensitivity to model representation of cloud processes, we carried out three sets of aqua planet simulations, which are labeled "CtrL" (control), "Cre0" (turning off cloud radiative effect, CRE), and "Ent0" (turning off subgrid-scale entrainment at cloud tops in the boundary layer).

1. The CtrL case is the standard configuration with all parameters set as default in HiRAM. The surface albedo in the CtrL runs is 17.3%.
2. The Cre0 case is the same as CtrL except that the CRE is switched off, artificially making the clouds transparent to radiation. The Cre0 simulations are analogous to those in the Clouds On-Off Klimate Intercomparison Experiment (COOKIE, see Fermepin & Bony, 2014; Stevens et al., 2012). The purpose of the Cre0 runs is to demonstrate that the change in the radiative heating ΔQ_{rad} forces cloud rapid adjustment regardless whether clouds affect Q_{rad} or not. The surface albedo in the Cre0 runs is 30.7%.
3. The Ent0 case is the same as CtrL except that the boundary layer turbulent mixing scheme (Lock et al., 2000) is turned off. As a result, any entrainment and detrainment between the clouds and the environment in the boundary layer occur only on the resolved grid scale. The surface albedo in the Ent0 runs is 2.5%.

Acknowledgments
We thank GFDL for making HiRAM available and Lucas Harris for helping with the earlier implementation of HiRAM. The computing resources for this project were provided by GFDL and the New Zealand eScience Infrastructure (NeSI). The data of the simulations that we carried out using HiRAM are available at https://doi.org/10.17608/k6.auckland.10252472. The data of the AMIP and AMIP4×CO_2 experiments were downloaded from the CMIP5 data archive at https://cera-www.dkrz.de/. We thank Tim Merlis and an anonymous reviewer for their comments and suggestions, which improve this manuscript. We acknowledge support from the National Science Foundation under Grant No. AGS-1743753.

References

Allen, M. R., & Ingram, W. J. (2002). Constraints on future changes in climate and the hydrologic cycle. *Nature*, *419*, 224–232. https://doi.org/10.1038/nature01092

Andrews, T., & Forster, P. M. (2008). CO_2 forcing induces semi-direct effects with consequences for climate feedback interpretations. *Geophysical Research Letters*, *35*, L04802. https://doi.org/10.1029/2007GL032273

Andrews, T., & Forster, P. M. (2010). The transient response of global-mean precipitation to increasing carbon dioxide levels. *Environmental Research Letters*, *5*(2), 025212. https://doi.org/10.1088/1748-9326/5/2/025212

Andrews, T., Gregory, J. M., Webb, M. J., & Taylor, K. E. (2012). Forcing, feedbacks and climate sensitivity in CMIP5 coupled atmosphere-ocean climate models. *Geophysical Research Letters*, *39*, L09712. https://doi.org/10.1029/2012GL051607

Bala, G., Caldeira, K., & Nemani, R. (2009). Fast versus slow response in climate change: Implications for the global hydrological cycle. *Climate Dynamics*, *35*(2-3), 423–434. https://doi.org/10.1007/s00382-009-0583-y

Betts, A. K., & Ridgway, W. (1988). Coupling of the radiative, convective, and surface fluxes over the equatorial Pacific. *Journal of the Atmospheric Sciences*, *45*(3), 522–536. https://doi.org/10.1175/1520-0469(1988)045h0522:COTRCAi2.0.CO;2

Blossey, P. N., Bretherton, C. S., Cheng, A., Endo, S., Heus, T., Lock, A. P., & van der Dussen, J. J. (2016). CGILS Phase 2 LES intercomparison of response of subtropical marine low cloud regimes to CO_2 quadrupling and a CMIP3 composite forcing change. *Journal of Advances in Modeling Earth Systems*, *8*, 1714–1726. https://doi.org/10.1002/2016MS000765

Bony, S., Bellon, G., Klocke, D., Sherwood, S., Fermepin, S., & Denvil, S. (2013). Robust direct effect of carbon dioxide on tropical circulation and regional precipitation. *Nature Geoscience*, *6*, 447–451. https://doi.org/10.1038/ngeo1799

Cao, L., Bala, G., & Caldeira, K. (2012). Climate response to changes in atmospheric carbon dioxide and solar irradiance on the time scale of days to weeks. *Environmental Research Letters*, *7*(3), 034015. https://doi.org/10.1088/1748-9326/7/3/034015

Cess, R. D., & Potter, G. L. (1988). A methodology for understanding and intercomparing atmospheric climate feedback processes in general circulation models. *Journal of Geophysical Research*, *93*(D7), 8305–8314. https://doi.org/10.1029/JD093iD07p08305

Chung, E. S., & Soden, B. J. (2018). On the compensation between cloud feedback and cloud adjustment in climate models. *Climate Dynamics*, *50*(3-4), 1267–1276. https://doi.org/10.1007/s00382-017-3682-1

Dinh, T., & Fueglistaler, S. (2017). Mechanism of fast atmospheric energetic equilibration following radiative forcing by CO_2. *Journal of Advances in Modeling Earth Systems*, *9*, 2468–2482. https://doi.org/10.1002/2017MS001116

Dong, B., Gregory, J. M., & Sutton, R. T. (2009). Undestanding land-sea warming contrast in response to increasing greenhouse gases. Part I: Transient adjustment. *Journal of Climate*, *22*(11), 3079–3097. https://doi.org/10.1175/2009JCLI2652.1

Fermepin, S., & Bony, S. (2014). Influence of low-cloud radiative effects on tropical circulation and precipitation. *Journal of Advances in Modeling Earth Systems*, *6*, 513–526. https://doi.org/10.1002/2013MS000288

Folkins, I., Fueglistaler, S., Lesins, G., & Mitovski, T. (2008). A low-level circulation in the tropics. *Journal of the Atmospheric Sciences*, *65*, 1019–1034. https://doi.org/10.1175/2007JAS2463.1

Gregory, J. M., Ingram, W. J., Palmer, M. A., Jones, G. S., Stott, P. A., Thorpe, R. B., et al. (2004). A new method for diagnosing radiative forcing and climate sensitivity. *Geophysical Research Letters*, *31*, L03205. https://doi.org/10.1029/2003GL018747

Gregory, J. M., & Webb, M. (2008). Tropospheric adjustment induces a cloud component in CO_2 forcing. *Journal of Climate*, *21*(1), 58–71. https://doi.org/10.1175/2007JCLI1834.1

Hansen, J. (2002). Climate forcings in Goddard Institute for Space Studies SI2000 simulations. *Journal of Geophysical Research*, *107*(D18), 4347. https://doi.org/10.1029/2001jd001143

Hansen, J., Sato, M., Ruedy, R., Nazarenko, L., Lacis, A., Schmidt, G. A., et al. (2005). Efficacy of climate forcings. *Journal of Geophysical Research*, *110*, D18104. https://doi.org/10.1029/2005JD005776

Harris, L. M., & Lin, S.-J. (2014). Global-to-regional nested grid climate simulations in the GFDL high resolution atmospheric model. *Journal of Climate*, *27*(13), 4890–4910. https://doi.org/10.1175/JCLI-D-13-00596.1

Kamae, Y., & Watanabe, M. (2012). On the robustness of tropospheric adjustment in CMIP5 models. *Geophysical Research Letters*, *39*, L23808. https://doi.org/10.1029/2012GL054275

Kamae, Y., & Watanabe, M. (2013). Tropospheric adjustment to increasing CO_2: Its timescale and the role of land-sea contrast. *Climate Dynamics*, *41*, 3007–3024. https://doi.org/10.1007/s00382-012-1555-1

Kamae, Y., Watanabe, M., Ogura, T., Yoshimori, M., & Shiogama, H. (2015). Rapid adjustments of cloud and hydrological cycle to increasing CO_2: A review. *Current Climate Change Reports*, *1*(2), 103–113. https://doi.org/10.1007/s40641-015-0007-5

Lock, A. P., Brown, A. R., Bush, M. R., Martin, G. M., & Smith, R. N. (2000). A new boundary layer mixing scheme . Part I: Scheme description and single-column model tests. *Monthly Weather Review*, *128*(9), 3187–3199. https://doi.org/10.1175/1520-0493(2000)128<3187:ANBLMS>2.0.CO;2

Medeiros, B., Stevens, B., & Bony, S. (2015). Using aquaplanets to understand the robust responses of comprehensive climate models to forcing. *Climate Dynamics*, *44*(7-8), 1957–1977. https://doi.org/10.1007/s00382-014-2138-0

Merlis, T. M. (2015). Direct weakening of tropical circulations from masked CO_2 radiative forcing. *Proceedings of the National Academy of Sciences of the United States of America*, *112*(43), 13,167–13,171. https://doi.org/10.1073/pnas.1508268112

Mitchell, J. F. B., Wilson, C. A., & Cunnington, W. M. (1987). On CO_2 climate sensitivity and model dependence of results. *Quarterly Journal of the Royal Meteorological Society*, *113*, 293–322. https://doi.org/10.1002/qj.49711347517

O'Gorman, P. A., Allan, R. P., Byrne, M. P., & Previdi, M. (2012). Energetic constraints on precipitation under climate change. *Surveys in Geophysics*, *33*, 585–608. https://doi.org/10.1007/s10712-011-9159-6

O'Gorman, P. A., & Schneider, T. (2009). The physical basis for increases in precipitation extremes in simulations of 21st-century climate change. *Proceedings of the National Academy of Sciences of the United States of America*, *106*(35), 14,773–14,777. https://doi.org/10.1073/pnas.0907610106

Pendergrass, A. G., & Hartmann, D. L. (2014). The atmospheric energy constraint on global-mean precipitation change. *Journal of Climate*, *27*(2), 757–768. https://doi.org/10.1175/JCLI-D-13-00163.1

Pincus, R., Forster, P. M., & Stevens, B. (2016). The Radiative Forcing Model Intercomparison Project (RFMIP): Experimental protocol for CMIP6. *Geoscientific Model Development*, *9*(9), 3447–3460. https://doi.org/10.5194/gmd-9-3447-2016

Ringer, M. A., Andrews, T., & Webb, M. J. (2014). Global-mean radiative feedbacks and forcing in atmosphere-only and coupled atmosphere-ocean climate change experiments. *Geophysical Research Letters*, *41*, 4035–4042. https://doi.org/10.1002/2014GL060347

Schneider, T., O'Gorman, P. A., & Levine, X. J. (2010). Water vapor and the dynamics of climate change. *Reviews of Geophysics*, *48*, RG3001. https://doi.org/10.1029/2009RG000302

Shine, K. P., Cook, J., Highwood, E. J., & Joshi, M. M. (2003). An alternative to radiative forcing for estimating the relative importance of climate change mechanisms. *Geophysical Research Letters*, *30*(20), 2047. https://doi.org/10.1029/2003GL018141

Stevens, B., Bony, S., & Webb, M. (2012). Clouds On-Off Klimate Intercomparison Experiment (COOKIE). www.euclipse.eu/downloads/Cookie.pdf

Takahashi, K. (2009). Radiative constraints on the hydrological cycle in an idealized radiative-convective equilibrium model. *Journal of the Atmospheric Sciences*, *66*(1), 77–91. https://doi.org/10.1175/2008JAS2797.1

Taylor, K. E., Stouffer, R. J., & Meehl, G. A. (2012). An overview of CMIP5 and the experiment design. *Bulletin of the American Meteorological Society*, *93*, 485–498. https://doi.org/10.1175/BAMS-D-11-00094.1

Vial, J., Dufresne, J. L., & Bony, S. (2013). On the interpretation of inter-model spread in CMIP5 climate sensitivity estimates. *Climate Dynamics*, *41*, 3339–3362. https://doi.org/10.1007/s00382-013-1725-9

Webb, M. J., Lambert, F. H., & Gregory, J. M. (2013). Origins of differences in climate sensitivity, forcing and feedback in climate models. *Climate Dynamics*, *40*, 677–707. https://doi.org/10.1007/s00382-012-1336-x

Wyant, M. C., Bretherton, C. S., Blossey, P. N., & Khairoutdinov, M. (2012). Fast cloud adjustment to increasing CO_2 in a superparameterized climate model. *Journal of Advances in Modeling Earth Systems*, *4*, M05001. https://doi.org/10.1029/2011MS000092

Xu, K.-M., Li, Z., Cheng, A., & Hu, Y. (2018). Changes in clouds and atmospheric circulation associated with rapid adjustment induced by increased atmospheric CO_2: Amultiscale modeling framework study. *Climate Dynamics*, 1–17. https://doi.org/10.1007/s00382-018-4401-2

Yano, J.-I., Grabowski, W. W., & Moncrieff, M. W. (2002). Mean-state convective circulations over large-scale tropical SST gradients. *Journal of the Atmospheric Sciences*, *59*(9), 1578–1592. https://doi.org/10.1175/1520-0469(2002)059<1578:MSCCOL>2.0.CO;2

Zelinka, M. D., & Hartmann, D. L. (2010). Why is longwave cloud feedback positive?. *Journal of Geophysical Research*, *115*, D16117. https://doi.org/10.1029/2010JD013817

Zelinka, M. D., Klein, S. A., Taylor, K. E., Andrews, T., Webb, M. J., Gregory, J. M., & Forster, P. M. (2013). Contributions of different cloud types to feedbacks and rapid adjustments in CMIP5. *Journal of Climate*, *26*, 5007–5027. https://doi.org/10.1175/JCLI-D-12-00555.1

Zhao, M., Held, I. M., Lin, S.-J., & Vecchi, G. A. (2009). Simulations of global hurricane climatology, interannual variability, and response to global warming using a 50-km resolution GCM. *Journal of Climate*, *22*, 6653–6678. https://doi.org/10.1175/2009JCLI3049.1